PHYSICAL SCIENCES: Earth, Atmospheric, and Planetary Sciences

# Biomass combustion produces ice-active minerals in biomass-burning aerosol and bottom ash

Leif G. Jahn[1,†,‡], Michael J. Polen[1,†,+], Lydia G. Jahl[1], Thomas A. Brubaker[1], Joshua Somers[1], Ryan C. Sullivan[1,*]

[1]Center for Atmospheric Particle Studies, Carnegie Mellon University, Pittsburgh, Pennsylvania, USA

[†]These authors contributed equally to the work

[+]Now at Department of Chemistry, McDaniel College, Westminster, Maryland, USA

[‡]Now at Department of Chemical Engineering, University of Texas at Austin, Austin, Texas, USA

*Correspondence to:*

Ryan C. Sullivan, Department of Chemistry, Department of Mechanical Engineering, 401 Scaife Hall, Carnegie Mellon University, Pittsburgh, PA, USA, 15213. (412) 268-8462, rsullivan@cmu.edu.

## Abstract

Ice nucleation affects the glaciation and evolution of clouds and their properties including radiative forcing and precipitation, yet the sources and properties of atmospheric ice nucleants are poorly constrained. Heterogeneous ice nucleation caused by ice nucleating particles (INPs) enables cloud glaciation at temperatures above the homogeneous freezing regime that starts near –35 °C. Biomass burning is a significant global source of atmospheric particles and a highly variable and poorly understood source of INPs. The nature of these INPs and how they relate to the fuel composition and its combustion are critical gaps in our understanding of the effects of biomass burning on the environment and climate. Here we show that the combustion process transforms inorganic elements naturally present in the biomass (not soil or dust) to form potentially ice-active minerals in both the bottom ash and emitted aerosol particles. These particles possess ice-nucleation activities high enough to be relevant to mixed-phase clouds and are active over a wide temperature range, nucleating ice up to –13 °C. Certain inorganic elements can thus serve as indicators to predict the production of ice nucleants from the fuel. Combustion-derived minerals are an important but understudied source of INPs in natural biomass-burning aerosol emissions in addition to lofted primary soil and dust particles. These discoveries should advance the realistic incorporation of biomass-burning INPs into atmospheric cloud and climate models. These mineral components produced in biomass-burning aerosol should be studied in relation to other atmospheric chemistry processes, such as facilitating multiphase chemical reactions and nutrient availability.

**Keywords:** Aerosol-cloud-climate interactions, atmospheric chemistry, heterogeneous ice nucleation, climate change, wildfires

## Statement of Significance

Ice nucleating particles significantly alter cloud properties and lifetime, causing large but poorly constrained climate impacts. Biomass-burning aerosol emitted by fires is a major and growing source of atmospheric pollution. Prior work suggested that ice nucleating particles can sometimes be emitted by biomass combustion, but the production and characteristics of these particles are poorly understood. Here we show that mineral phases are a significant ice-active component of both biomass-burning aerosol and ash particles. These mineral phases are derived from plant inorganic material that decomposes and reforms as ice-active minerals during combustion; they form more commonly from tall grass versus wood fuels. Aerosolized mineral and ash are now understood as a major source of the ice nucleating particles in biomass-burning smoke.

## Introduction

Ice nucleation (IN) and cloud glaciation have extensive effects on cloud microphysics and the evolution, structure, lifetime, precipitation, and radiative properties of clouds (1–3). Ice nucleating particles (INPs) compose a tiny fraction of atmospheric particle numbers. Typically 1 to 10 per 1 million ambient particles are found to be ice active at –30 °C under immersion freezing conditions – where the INP is immersed in a supercooled cloud droplet (4). Despite their scarcity, INPs exert significant effects on cloud evolution, largely driven by the scavenging of water from unfrozen droplets by ice crystals in mixed-phase clouds. Glaciation of supercooled liquid clouds dramatically reduces their visible optical depth and thus albedo (2, 3) while often initiating precipitation (1–3). Furthermore, climate models with different representations of glaciation have systematically different frozen fractions as well as climate sensitivities (5). Not only is the accurate representation of INPs essential to represent the current climate state, but a proper understanding

of potential changes to INPs due to human activity is essential to advance climate change modeling. However, accurate determination of INP sources, budgets, distributions, and the individual particle characteristics that affect ice nucleation are a significant challenge due to the overall scarcity of INPs. The nanoscale nature of heterogeneous ice nucleation and the associated ice-active surface sites that control this phase transition make this process challenging to directly observe (6).

Minerals are the most common type of atmospheric INPs and are typically ice-active below –15 °C, with wide variation in ice nucleation activity (INA) observed for different mineral phases (7). These ice-active minerals are found in atmospheric desert dust, soil, and volcanic ash particles and have important effects on regional and global scales (7–10). Biomass burning represents an important component of the global aerosol burden (11–15) and can be a major episodic and regional source of particulate matter (11, 13, 14, 16, 17). Biomass-burning aerosol (BBA) has been observed to undergo long-range transport (13, 15, 18) and to affect cloud properties by acting as cloud condensation nuclei (18–20) and INPs (18, 21, 22) over large regional extents. Changes in land use and climate at global and regional scales are predicted to increase the frequency, intensity, and scale of wildfires and prescribed burns over the coming years (23–27), making biomass-burning aerosol an even more important perturbation to the Earth's atmosphere and climate systems in the near future. Regions not historically prone to major wildfires, such as the southeastern United States, have recently experienced extensive drought-driven biomass burning events (28). The Australian bushfires of 2019-2020 represent the largest wildfire event in modern history (29), where tall grasses, shrubs, and other brush species as well as leaf litter constituted some of the major biomass fuels consumed. Our lack of understanding regarding the sources, properties, and even the chemical identity of INPs present in biomass smoke plumes has precluded their proper representation in chemical transport and cloud microphysical models (18).

Biomass burning is a complex process, producing aerosol (BBA) and ash particles composed of variable amounts of organic carbon, elemental carbon (soot), and inorganic phases (most commonly potassium salts). Elevated levels of INPs that freeze as warm as –16 °C are inconsistently observed in plumes from wildfires and prescribed burns, but the INP sources and particle types remain undetermined with no clear correlation to fuel type or combustion conditions (21, 22, 30, 31). Petters et al. found that INP concentrations at –30 °C in BBA correlated with aerosol potassium fraction, aerosol inorganic fraction, and modified combustion efficiency, and negatively with organic carbon fraction (21). While soluble inorganic salts are not expected to be ice active, each observed positive correlating factor is an indicator of higher-temperature flaming-phase combustion emissions. However, these correlating factors have not proven definitive in predicting INP production (18, 21, 31). The results of Petters et al. suggest that soot and other inorganic or mineral components may be the major contributor to INPs from biomass-burning emissions, or that hotter flaming combustion – which increases the inorganic fraction relative to the organic fraction in the aerosol phase (32, 33) – enhances the production of INPs. In prior studies, tall grass fuels such as wiregrass and sawgrass often produced particles with the highest observed ice-nucleation activity (INA) (21, 22). The cause of the greater INA of BBA from tall grasses versus wood was not determined, though the tendency of the tall grasses to combust more intensely under flaming conditions is one possible explanation (30, 31). Soot as a potential INP has also been suggested by measurements of ice-active particles sampled from biomass-burning plumes, with soot found in up to 50% of the ice crystal residuals (22, 31). However, fossil fuel combustion soot is generally a weak INP, typically lacking any measurable immersion freezing activity above approximately –25 °C (18, 34–36), and is unlikely to be relevant for mixed-phase

clouds. These studies on the INA of black carbon aerosol point to another, not clearly identified, component in BBA besides black-carbon soot acting as the major ice nucleant, particularly above –25 °C (18).

The lofting of ash, soil, or mineral dust particles during or following combustion (37–39) could account for INPs in BBA active above –25 °C, and explain differences between fuels and correlations between aerosol composition and freezing efficiency. Biomass ash – the refractory material produced through combustion – is mobilized by wind and precipitation following combustion events (39). Recent observations have shown that precipitation can loft soil and organic matter into the atmosphere (40, 41); such events could loft biomass ash through a similar mechanism. Biomass ash and soil particles emitted by biomass burning up to 1 mm in diameter have been observed at concentrations of >10 particles per $m^3$ of air (42, 43), while inorganics and metallic elements attributed to soil markers have been measured in wildfire smoke-influenced aerosol (44, 45). However, combustion of biomass is well known to produce a variety of new inorganic components and crystalline mineral phases (46, 47) which may cause ash particles to appear similar to mineral dust or soil particles if elemental markers are used for identification. These phases are produced directly by combustion from elements naturally present in biomass such as Si, Al, Ca, Mg, S, and K (48–51). Ash and aerosol composition depend on the elemental composition and nature of the source biomass material (46, 47, 52) as well as combustion characteristics, with higher temperature combustion producing more crystalline material (53–55). While these issues have been extensively evaluated in the biomass combustion literature, the potential role of biomass burning as a source of new ice-active mineral phases emitted to the atmosphere has not been fully explored or directly examined in the emitted aerosol particles. Combustion ash can be a source of INPs, as first observed through the combustion disintegration of a sugar cane leaf skeleton that released INPs and inorganic refractory particles (56). Recent studies have examined the INA of wood ash and observed moderate INA, with activity slightly weaker than common INP such as desert dusts (57, 58). These studies have also suggested inorganic mineral materials, rather than carbonaceous materials, as the source of ash INA. However, the ash generated in these studies may not be representative of what would form during natural combustion events, as ash samples were generated in domestic heating ovens that combust fuel in a controlled and efficient manner.

Here we investigate the ice nucleants produced in biomass-burning bottom ash and aerosol generated from the open-pan flaming combustion of grass and wood fuels relevant to the western and southeastern United States (59, 60). Globally, both grassland and forest fires contribute significantly to biomass-burning emissions (12, 61). Both grassland and forest biomes were major components of the area burned during the 2019-2020 Australian bushfires that represent the largest wildfire event in modern history. Investigation of BBA and ash in a laboratory setting allows for isolation of BBA from ambient background or lofted aerosol (22, 44) and chemical aging effects (13) that complicate ambient measurements of INPs in BBA. We observe immersion freezing to occur at temperatures as warm as –13 °C. We find that the INA of ash and aerosol can be related to the composition of the ash and aerosol and the new mineral phases produced, as well as that of the original biomass fuel.

While previous studies have characterized BBA composition and identified INA, an understanding of what drives the variability in INA between different fuels and what fuel or combustion properties drive the production of INPs have been major knowledge gaps (18). Here we have identified an important previously unrecognized relationship between the inorganic components in the fuel, the crystalline phases produced during the transformation of biomass fuel

to ash and aerosol, and the corresponding production of INPs in BBA. This new understanding of the sources and properties of INPs produced by biomass burning will significantly improve our understanding and model representations of INP budgets and transport, and mixed-phase cloud microphysics, both in smoke-impacted regions and on a global scale (5, 18).

## Results

*Ice-nucleation activity of biomass-burning aerosol and ash*

The INA of aerosols and ashes produced through biomass combustion was determined in the immersion mode using a droplet-on-substrate cold plate assay (62, 63). BBA was collected from a large Teflon chamber filled with diluted smoke from open pan combustion of 100-500 g of authentic wood or tall grass fuels collected in the conterminous United States; flaming combustion conditions were maintained during chamber filling (see Samples & Methodology). The ash produced was collected from the same pan. BBA and ash produced from tall grasses are more ice active than wood BBA and ash (Fig. 1), with freezing observed as warm as –13 °C in some ashes. Three of the four grass BBA samples freeze well above the background freezing spectrum of the filtered water control, with 50% of droplets frozen between –22 and –24 °C, while all of the woody BBA samples are not distinguishable from the background (Fig. 1 and SI Appendix, Fig. S1). The remaining grass BBA sample, switchgrass, possess weaker INA than the other grasses but still exhibits freezing above background at temperatures warmer than –20 °C (SI Appendix, Fig. S1).

We observe immersion freezing of BBA at temperatures up to –15 °C, which is comparable to ambient measurements of biomass smoke-impacted aerosol (22) and warmer than previous laboratory measurements that were limited to temperatures colder than –28 °C (31). The woody birch and fatwood fuels produce more soot than the grasses (SI Appendix, Fig. S5), suggesting that the soot components of BBA are not significant INPs in the fuels examined in this study. The tall grass BBA and ash also freeze at temperatures well above where combustion soot typically nucleates ice (34–36). For both the sawgrass and cutgrass fuels, the ice-active site density ($n_s$) – a commonly-used measure of INA – of the ash is greater than but comparable to that of the aerosol (Fig. 1). Birch ash possesses lower $n_s$ values than the other ashes indicating a lower concentration of ice nucleants. Droplet freezing and $n_s$ spectra for other fuels studied are included in SI Appendix, Figs. S1 & S2.

Several groups have recently examined the INA and composition of domestic wood and coal ashes and found each to be moderately ice active (57, 58, 64, 65), while our results are the first to target both fuels and conditions relevant to natural biomass combustion. These results, some of which are included in Fig. 1, are similar to ours with ash-induced freezing spanning –12 °C to –37 °C and $n_s$ values from $10^{-1}$ to $10^{2}$ cm$^{-2}$. The freezing temperatures and $n_s$ values observed for the BBA and ash produced from the tall grasses studied here possess similar or higher INA ($n_s$) than domestic wood ash. Coal fly ash has a much steeper rise in $n_s$ but starts at a slightly lower temperature than the biomass ashes reported here.

The ash samples freeze over a similar temperature range, from –16 °C to –30 °C, though several grass ashes (cutgrass and NC grass) start freezing at temperatures as warm as –13 °C. However, ashes also possess $n_s$ values that vary from $10^{-1}$ to $10^{4}$ over these temperatures, with most ashes (cutgrass, NC grass, wiregrass, switchgrass, and ponderosa pine) possessing similar $n_s$ values in the range of $10^{0.5}$ to $10^{2.5}$. Considering that $n_s$ can vary over a range of $10^{10}$ (7) and that typical measurement uncertainties or method differences cause variability in $n_s$ of $10^{1}$-$10^{2}$ (66, 67), these can be regarded as possessing similar INA. These freezing results together suggest a similar origin for the INA in the ash samples, but that the amount of ice-active material varies between

the ash samples. The above-mentioned prior studies on coal fly ash INA found a link between INA and mineral components, in particular calcium-bearing phases, with some possible contribution from silicon-bearing phases (64, 65), and are discussed further in the SI Appendix, Section 3. Our results are also the first to study the INA of ash from tall grasses and wood generated during open-pan flaming combustion that is more representative of how fuels combust in a variable and uncontrolled manner during natural wildfires and prescribed burns, as opposed to more controlled combustion in a stove or high-efficiency furnace. Immersion-freezing activity at temperatures similar to our BBA and ash in Fig. 1 has been observed for calcium minerals (68, 69) as well as quartz (69–71) and amorphous silica (70, 72). Nominally mineralogically similar quartz minerals were recently reported to possess widely varying INA that depend on the particle surface properties and environmental factors (71), indicating that the INA of silica mineral phases can be higher and more variable than previously understood.

*Ash composition and relationship to ice nucleation activity*

The INA of biomass-burning ash likely results from ice-active calcium and silicon-based mineral phases. These types of phases are observed in the X-ray diffraction (XRD) spectra of each ash sample (Fig. 2), and are similar to some of the phases observed in prior work (57). Stronger ash INA is also associated with higher amounts of crystalline material in the ash, with ashes composed of more amorphous material possessing weaker INA. Similar associations between INA and increasing crystallinity have also been observed with alumina minerals (73). The weaker INA of the birch ash could also be due to greater amounts of organic carbon material, which has generally been shown to be an ineffective ice nucleant in the immersion mode over this temperature range (10, 21). These associations are also consistent with the composition of the ash and unburnt fuels, as birch wood and ash contain 10-1000 times less calcium and silicon compared to those from tall grass fuels (Table 1). This would suggest that combustion of birch has a smaller potential to produce ice-active mineral phases, and a correspondingly lower INA results (Fig. 1).

Despite similar fuel characteristics and combustion procedures, combustion of cutgrass, sawgrass, switchgrass, and the NC grass produces ash with varying amounts of crystalline phases and amorphous material. The reason for this difference is unclear but illustrates the variability inherent to biomass-burning emissions. Some grass ashes contain quartz ($SiO_2$) and all likely contain amorphous silica phases, as the grass ashes analyzed contain large amounts of silicon. The INA of both quartz and amorphous silica has previously been linked to grinding of the sample that may create ice-active surface sites (70, 72), and we ground our ash samples prior to INP analysis. The aerosol samples were not ground, however, and were simply extracted off the filter into water yet still exhibit INA similar to though somewhat lower than the ashes (Fig. 1). Both our aerosol and ash samples exhibit INA similar to the range reported for quartz minerals (71).

The mineral phases present in the combustion particles likely possess surfaces that are topographically and chemically diverse and also distinct from those of pure mineral standards (70–72) or synthesized commercial products (70, 72) that have been used in prior analyses due to the energetic non-equilibrium and variable formation conditions within a complex matrix that are characteristic of natural biomass combustion. Thus, these combustion-derived minerals may possess the surface chemical characteristics (70) and higher-energy topographical features and defects (6) that are associated with mineral ice nucleants without further treatment or grinding. Many crystalline phases can be produced in bottom ash (46), and XRD is a bulk analysis technique that will not detect phases present in small amounts. Scarcer mineral phases that possess greater ice activity would not be identified in our XRD analysis but could still play important roles in driving the INA of the ashes.

*Prevalence and characteristics of aerosol mineral phases*

We investigated the prevalence of ice nucleation-relevant mineral phases in BBA by analyzing the individual particle composition of cutgrass, sawgrass, and ponderosa pine BBA samples using computer-controlled scanning electron microscopy (CCSEM; SI Appendix, Table S1). Some amount of calcium, silicon, and particles containing mineral inclusions (>1.0 atomic % of magnesium, aluminum, silicon, calcium, manganese, iron, and zinc) are present in the BBA from all three fuels, though larger amounts are present in grass BBA. CCSEM results show that 3.4% of ponderosa pine particles contain mineral inclusions while 17.4% and 11.9% of cutgrass and sawgrass particles, respectively, contain mineral inclusions. The presence of these refractory inorganic elements is consistent with previous measurements of BBA composition (74–76). Even small amounts of silicon may be significant, as silicon was a minor component of many ice crystal residuals identified in ambient BBA plumes (22). The exact phase of these elements is unclear, however crystalline and polycrystalline or amorphous phases were observed in transmission electron microscopy analysis of BBA (Figs. 3 and 4). Further discussion of the detection and analysis of mineral phases using TEM is provided in the SI Appendix, Sections 1 and 4. The INA of such phases is unknown but their presence demonstrates the potential for combustion-produced crystalline or amorphous mineral phases to be present in BBA as well as bottom ash.

The nature of the mineral phases present in the aerosol and ash are likely different, as the ash particles that become lofted are likely on the smaller end of the potential size range for ash particles and these particles may differ from the bulk ash composition. Potassium-bearing crystalline phases are also present in these aerosols, similar to prior measurements (75), but the relatively high water solubility of these salts renders them less directly relevant to INA. While potassium has been used as a marker for BBA in ambient samples (75), it may not be a reliable indicator of INPs in BBA considering that almost all biomass fuels produce significant potassium in BBA, while only some fuels produce INPs (21, 22, 30, 31). The reliability of potassium as a marker for BBA in ambient samples arises because potassium is present in almost all plant material (50, 51, 77) that is easily volatilized during combustion and then condenses onto particles (51). The correlations observed in lab measurements between aerosol potassium content and number of INPs likely occur for two reasons. First, hotter and more intense combustion will volatilize more potassium while also leading to more mineral transformations and potentially increased lofting of fly ash aerosol. Second, in our work fuels with more potassium also tended to be enriched in other inorganic elements like calcium and silicon (Table 1). This association between high fuel potassium content and high inorganic mineral content is consistent with literature measurements (49) and indicates that these inorganic-rich fuels have a greater potential to form ice-active mineral phases.

Carbonaceous particles with small amounts of silicon have been observed in wildfire plumes (75, 78) and in ice crystal residuals sampled from plumes (22), and could be generated through different mechanisms. Unburnt or partially combusted biomass materials containing inorganic elements can be lofted during combustion but have been observed in greater amounts during smoldering-phase combustion (76), suggesting these are not a significant source of INPs (21, 30, 31). Inorganic elements transformed through combustion into mineralized material can be lofted during combustion, akin to the lofting of soil particles or fly ashes (79–82). Elements volatilized during combustion will condense to form particulate inorganic phases. This is widely observed for volatile elements such as potassium (75, 76, 82, 83) and to lesser extents for less volatile elements such as calcium and silicon (82–84) that are likely only to volatilize from aqueous or organically-bound biogenic phases (46, 80, 82, 85–88), which has been observed over a wide

temperature range (46). Si-bearing combustion INPs may originate from ash breakup and lofting or from the deposition of volatilized biogenic silicon. In the latter case, these Si-containing regions could potentially create ice-active sites on soot particles which are otherwise weakly IN-active. The formation and lofting of inorganic phases by biomass burning are discussed further in the SI Appendix, section 6.

To our knowledge these are the first results that posit the production or release of new mineral phases through combustion as the main source of the INA of BBA and ash, and to connect this INA with the composition of the original biomass fuel. This addresses the long-standing knowledge gap regarding the underlying causes behind the large variability in the INA of BBA produced from different biomass fuels, or even whether ice nucleating particles are or are not emitted. The fact that our results point to pyrogenic mineral phases as ice nucleants in BBA and ash may explain the variability and inconsistency of prior INP measurements in BBA. While many types of fuels take up similar elements in similar amounts, this isn't universal among fuels we regard as being similar. For example, the ICP-AES analysis of our cutgrass, NC grass, switchgrass, and wiregrass fuels (Table 1) show different amounts of almost all of the elements analyzed, despite these all being species of tall grass. The presence of inorganic elements such as calcium and silicon that are able to form ice-active mineral phases (64, 65, 68, 71, 89) can serve as a broad indicator of whether ice-active minerals may be produced in BBA and ash.

In our work fuels with higher calcium and silicon content tended to produce more ice nucleants in either or both the aerosol and ash phases, as woody fuels with relatively small amounts of calcium and silicon produced BBA and ash with fewer and weaker ice nucleants compared to grassy fuels. The presence of these elements varies between different types of fuels and within different parts of the plant, and can also vary with growth stage, soil content, and in response to environmental conditions (48–50, 90). The observed association between more silicon and calcium in the biomass fuel and higher ash or aerosol INA holds for most but not all biomass samples we tested. This is unsurprising as biomass combustion in a complex process with many factors potentially affecting the production of ice-active minerals, such as the chemical forms of silicon and calcium within biomass, the combustion temperature, how the combustion products partition between the aerosol and bottom ash, and where within the fire and at what point during the fire's history this partitioning occurs. Finding a single factor that accurately predicts INP production or any other property of the complex BBA during all biomass combustion scenarios is likely not feasible, as has been concluded in prior studies (13, 21, 22, 31, 91).

Here we propose a new framework wherein the higher-temperature (warmer than ~ –25 °C) INA of biomass-burning ash and aerosol is now understood to be largely driven by new mineral phases produced by combustion, which is largely governed by the fuel composition and its combustion conditions. This new model should allow the ice nucleation properties of BBA to be understood in terms of the mineral components present, meaning the large existing body of research on mineral-based ice nucleants is also relevant to biomass burning. This will facilitate the more accurate inclusion of INPs from biomass burning in atmospheric models and provides a new perspective on which to base predictions of the emissions of INPs and their underlying minerals from wildfires and biomass combustion.

*Potential contribution of lofted soil to measured INPs*

INA of soil particles has previously been attributed to both organic/biomolecular and mineral components (92, 93), and XRD analysis of the soil collected with the NC grass shows that it contains ice-active alkali feldspar and quartz mineral phases (SI Appendix, Fig. S8). Unburnt soil was found to contain ice-active components with 50% droplets frozen by –15 °C, but soil

particles exhibit a substantial though incomplete reduction in their INA following combustion (Fig. 1 & SI Appendix, Fig. S5). Alkali feldspars are the most ice-active mineral phases known and likely explain the freezing observed in the soil, given the overlap with the K-feldspar $n_s$ spectrum (Fig. 1). Ice-active organic or biological components of soil would not be expected to survive biomass combustion, and our results indicate that the INA of soil mineral components can be decreased by combustion (Fig. 1). XRD analysis indicates that the bulk mineral composition remains unchanged, but this analysis would be insensitive to mineralogical changes that occur at or near particle surfaces that may affect ice nucleation. Due to the significant observed decrease in $n_s$ values, we suspect that a combination of heat and chemical reactants generated during combustion alters the surfaces of mineral phases in a manner that degrades ice-active sites. This is further evidence that the INA of biomass-burning aerosol and ash has a significant contribution from newly produced mineral phases and is not predominantly driven by pre-existing soil or dust particles lofted during combustion. The biomass fuels used here were harvested from above the topsoil level and did not contain notable amounts of soil or dust. While these pre-existing mineral ice nucleants can survive the combustion process, their INA appears to be reduced appreciably, particularly at the warmer freezing temperatures above –20 °C.

## Atmospheric Implications

The mineral phases directly produced by biomass combustion represent an unrecognized source of mineral-containing particles to the atmosphere, in addition to the primary soil and dust particles suspended by wildfires. The INA of biomass ash and aerosol appear directly related to the ability of the fuel to decompose during combustion to form or release ice-active mineral phases, which is in turn based on the composition of the biomass fuel and the combustion intensity. These newly produced mineral phases exhibit significant INA within the range of other known mineral phases, potentially simplifying the description of these particles and their effects on clouds and climate in atmospheric models. The potentially ice-active mineral phases observed in this work – quartz, amorphous silica, and calcium carbonate – are consistent with past observations of combustion-derived mineral phases (39, 46, 47, 57). This also provides further evidence that under immersion freezing conditions warmer than roughly –25 °C, atmospheric ice nucleants are predominantly derived from either mineral phases with an upper freezing temperature range of –15 to –10 °C (8, 10), or from macromolecules and other biological components that can nucleate ice as warm as a few degrees below 0 °C (10, 94).

Previous variability in laboratory (21, 31) and ambient (22, 30) measurements of INPs in BBA likely relates both to the variability in the production of mineral phases through combustion among similar fuels, the combustion phase and intensity that the emissions were sampled from, and variability in lofted pre-existing soil or dust components. Soil matter that becomes lofted during biomass combustion events is susceptible to a reduction in its INA due to the heat and chemical transformation processes that produce and transform ash material. Tall grasses are a major type of fuel for biomass-burning events globally (12, 95), and our results suggest that grass fires consuming fuels with larger amounts of silicon and calcium are more significant than wood fires for the generation of INPs relevant to inducing glaciation under mixed-phase cloud conditions above ~ –35 °C. This suggests that the INA of biomass combustion particles should have significant regional variation based largely on fuel type, consistent with the variation in other properties of BBA (96), and can better inform how the budget and characteristics of INPs from biomass burning are represented in models on a regional and global scale. A more robust identification of the origin of in-plume inorganic and mineral particles together with ambient measurements following biomass-burning events will advance our understanding and constraints

on the prevalence of biomass-derived minerals and ash as atmospheric aerosols, and their resulting effects on cloud microphysics, nutrient transport, and geochemistry (97, 98).

A potentially important consequence of this new perspective regarding the source of INPs from biomass burning is that mineral particles measured in ice crystal residues could be mistakenly attributed to long-range transported desert mineral dust instead of their actual source from biomass-burning produced ash or aerosol, or entrained soil dust. This would misinform the sources, abundance, atmospheric distribution, and transport of INPs and their representation and effects on cloud microphysics, radiation, precipitation, and climate in atmospheric chemical transport and climate models. While desert dust, soil particles, and volcanic ash have previously been considered to be major sources of atmospheric mineral phases and their associated ice nucleants, biomass burning should also be considered as a significant and episodic source of ice-active minerals to the atmosphere.

To estimate the number of INP emitted by biomass burning and over what regional extent in the atmosphere this may produce elevated INP concentrations above typical background levels, we followed the initial model developed by Petters et al. (21). At –25 ºC a range of $5x10^{10}$–$1x10^{12}$ INP/L air per $m^2$ burned can be emitted based on the tall grass experiments (see the SI Appendix for further details). Considering $n_{INP} > 1$ per L of air to be above typical background levels at –25 ºC and a plume height rise of 5 km, the plume could spread from 1 $m^2$ burned over an horizontal area up to 100 km × 100 km and still introduce INP number concentrations of ≥ 1 per L air per $m^2$ burned. Large wildfires may consume 1000s of $km^2$ in area per week, introducing massive amounts of BBA into the atmosphere, though the ice activity of the aerosol would depend in part on the type of fuel burned, among other factors (21). A more comprehensive understanding of the contribution of INPs from biomass burning and their impacts on cloud microphysics requires proper inclusion of this emerging source of INPs into chemical transport and cloud models.

## Samples and Methodology

*Preparation and collection of biomass-burning aerosol and bottom ash samples*

Ash and aerosol samples were collected from biomass burns performed in the Carnegie Mellon University (CMU) combustion facility within the Air Quality Laboratory (99). For each burn approximately 500 g of fuel was weighed in a galvanized steel pan that also held the sample during combustion. Fuels did not appear to contain any residual soil or other material but were not cleaned prior to combustion. Residual duff was separated from the target fuel for each burn. Between burns the pan was emptied and thoroughly rinsed with MilliQ water. Roughly a third of the fuel mass was lit on fire with a butane igniter and allowed to burn until the flames began to die down. Then, the rest of the weighed fuel was gradually added to maintain visible flaming-phase combustion until it was all consumed, lasting 5-10 minutes. Three to five fuel additions were performed for each sample, depending on the density of the fuel. The grasses and pine needles and branches were less dense than birch or fatwood and burned, so more additions were performed. The grasses tended to burn more quickly than the woody fuels, overall. Among the grasses, wiregrass burned more slowly than sawgrass, cutgrass, and switchgrass, while among the woody fuels ponderosa pine needles and branches burned more quickly than birch or fatwood. Flaming-phase combustion is described by a high modified combustion efficiency approaching unity, indicating near complete combustion of the fuel to $CO_2$ and $H_2O$ that results in a greater fraction of the fuel being converted to thermal energy. Finally, the fire was allowed to extinguish itself and cool. The temperature of the fire was not monitored during the experiment. This method was used to simulate to the best of our ability flaming-phase combustion conditions and its transition through

smoldering-phase to extinction that occurs during natural biomass burning events (that is, wildfires and prescribed burns).

Ash samples were transferred with tongs from the pan to new zippered plastic bags and sealed until analysis. During combustion, the smoke emissions were injected and diluted using Dekati eductor diluters (Dekati DI-1000) into a 12 $m^3$ Teflon smog chamber partially filled with clean particle-filtered air (99). Online chamber aerosol composition measurements were acquired using a soot-particle aerosol mass spectrometer (Aerodyne, Inc.). The aerosol size distribution for particle mobility diameters 14-736 nm was characterized with a differential mobility analyzer (TSI, model 3080) and condensation particle counter (TSI, model 3772) acting as a scanning mobility particle sizer (SMPS). Representative size distributions are shown in the SI Appendix, Fig. S10 and were taken one hour after the start of each burn, corresponding to the halfway point of particle sampling for INA analysis. The chamber smoke aerosol was subsequently collected on 50 nm pore size nuclepore filters (GE Healthcare #111103) in an inline filter holder with no prior size segregation for analysis of the BBA. Filter sampling began 1-2 minutes after smoke injection into the chamber finished and then lasted for 1-2 hours. Burn characteristics, including as initial fuel mass, chamber aerosol loadings, and sampling time are listed in SI Appendix, Table S2.

Particles larger than 700 nm will not be measured by the SMPS but will be collected for INA analysis, biasing measured surface area low and calculated $n_s$ values high. However, based on the measured size distributions for each aerosol population and the low measured number of particles (<1%) with electrical mobility diameter 500–700 nm (SI Appendix, Fig. S10), we conclude that the contribution of particles with electrical mobility diameter >700 nm to the total particle population will be small and will not significantly impact our results. The discrepancy between measured and sampled surface areas would need to be more than an order of magnitude to significantly impact our log-space $n_s$ results such as shown in Figs. 1 and SI Appendix, Fig. S2.

Fuels included giant cutgrass (*zizaniopsis miliacea*, collected at the UF/IFAS Center for Aquatic and Invasive Plants, Florida, USA); sawgrass (*claudium mariscoides*, collected at the UF/IFAS Center for Aquatic and Invasive Plants, Florida, USA); untreated birch wood (purchased from a local hardware store, Pittsburgh, PA, USA); pine fatwood (purchased from a local hardware store, Pittsburgh, PA, USA); ponderosa pine needles and branches (*pinus ponderosa*, Klamath Basin National Wildlife Refuge Complex Tulelake, CA, abbreviated as pon. pine); switchgrass (*panicum virgatum,* cultivated by Phipps Conservatory, Pittsburgh, PA, USA); wiregrass (*aristida beyrichiana*, Okefenokee National Wildlife Refuge, Georgia, USA); and an unidentified wetland grass (Alligator River National Wildlife Refuge, North Carolina, USA, referred to as NC grass). Grass fuel samples were collected when green and stored at ambient conditions in the laboratory for 6-12 months prior to burning, causing fuels to dry out to an extent; birch and fatwood were purchased as a dry wood. Naturally occurring biomass also dries depending on the season and weather, and typically only burns when the fuel itself is relatively dry. The soil sample was collected in the same location in North Carolina as the unidentified wetland grass. For one experiment (birch + soil), the fuel was weighed and burned the same way, but 220 g of fuel was used and 6.5 g of soil was sprinkled over the fuel in the pan immediately before burning.

Ash samples were lightly ground with a mortar and pestle and then sieved to less than 63 μm (U.S.A. Standard Testing Sieve, Fischer Scientific) by putting the sieve in an ultrasonic bath. Ash particles larger than approximately 0.5 cm were avoided during grinding. Grinding and sonicating may break up particles and particle aggregates, but this type of breakup can also occur due to natural processes driven by wind, saltation, or precipitation and weathering. Particles larger and smaller than 63 μm were stored in separate 50 mL plastic Falcon tubes. Only the sub-63 μm

samples were analyzed for this study due to the very short atmospheric lifetimes of even larger particles. For immersion freezing measurements 0.001 mg of ash sample was suspended in 10 mL of filtered HPLC-grade water to create a 0.01 wt% suspension.

*Droplet freezing assays to determine ice nucleation activity*

Ice nucleation activity (INA) and the cumulative INP concentration versus temperature spectra were determined using the Carnegie Mellon University cold stage (CMU-CS) "droplet-on-substrate" immersion freezing technique described by Polen et al. (63, 100). Briefly, sample suspensions are prepared from HPLC-grade water (Sigma Aldrich HPLC Plus #34877) that was filtered (Anotop 25 Plus 0.02 μm pore size, Whatman #6809-4102). We have found filtering HPLC-grade bottled water with a 0.02 μm Anotop filter provides the lowest and most consistent background freezing spectra (63). Droplets containing particles are pipetted onto a silanized hydrophobic cover slip (Hampton Research, HR3-231) immersed in squalene oil (TCI chemicals, #H0097) in an aluminum sample dish. The dish sits atop a thermoelectric cooling element that provides fine temperature control. A three-stage thermoelectric air chiller is used as a heat sink. Droplet temperature measurements have an uncertainty of ±0.5 °C. Approximately 40-50 droplets with a volume of 0.1 μL (or 25-35 droplets with a volume of 0.5 μL) are deposited into the oil using a micropipette. Droplet images are acquired every 5-6 seconds using a CMOS camera as the array is cooled at 1 °C/min, and freezing is detected based on the change in the grayscale value using a custom Matlab program that also determines the droplet diameter (101). Two to four arrays were acquired for each sample, depending on the number of droplets in each array. The conventional cold plate assay experiences background freezing of filtered water droplets starting around –25 °C; this determines the range of observable freezing temperatures. The freezing temperature spectrum of filtered water droplets was routinely measured. Collected aerosol samples were suspended by vortexing the nuclepore filter in a plastic falcon tube with 3 mL of filtered water. Freezing assays were then performed as above with this suspension.

Droplet freezing spectra were acquired for each array and then converted to ice-active surface site density (102, 103), more commonly referred to as $n_s$. Prior to the conversion to $n_s$, the average ice nuclei concentration ($c_{IN}$) spectrum for the filtered water controls was subtracted from the $c_{IN}$ spectrum of each sample (104) to account for interference from background freezing due to trace water impurities or droplet–substrate interactions (63). For some samples this causes $n_s$ values to decrease or become negative towards lower temperatures, and where applicable we have truncated spectra below this temperature as we cannot resolve the heterogeneous ice nucleation from the background freezing at these points.

*Particle analysis methods*

Brunauer-Emmett-Teller (BET) surface area analysis was performed on the ground and sieved < 63 μm ash particles to determine bulk ash particle surface area using $N_2$ gas adsorption (Gemini VII 2390, Micromeritics) and is reported with other sample characteristics in Table 1. The measured BET surface area-to-mass ratio was used to compute the ice active surface site density ($n_s$) metric that normalizes for particle surface area (62, 63, 102). Total surface area for collected aerosol samples was determined from the total air volume collected by the filter (flow rate measured in-line with a Gilibrator) and the aerosol size distribution measured by a scanning mobility particle sizer (TSI, Model 3080 DMA and 3772 CPC), assuming spherical particles with a density of 1 g $cm^{-3}$. X-ray diffraction (XRD) measurements were performed on a PANalytical X'Pert Pro MPD diffractometer. A copper X-ray source was used, and all scans were done over the °2θ range of 10°-70° with a step size of 0.013°. XRD was used to identify the crystalline/mineral phases present in the ash and soil samples using the closest matching spectra

available in the crystallography open database (COD) and the International Centre for Diffraction Data (ICDD) database. For the soil and some ash samples, a Rietveld refinement was used to determine the relative amounts of the identified crystalline phases. Elemental analysis using ICP-OES following borate fusion was performed by Huffman Hazen Laboratories (Golden, Colorado, USA) on bottom ash and on unburnt fuel samples and are reported on a per weight basis in Table 1. Ash content – measured as the mass of refractory material remaining following ashing – was also measured for each of the unburnt fuel samples and is reported in Table 1.

Particles were sampled onto copper formvar TEM grids (carbon type B, 400 mesh, Ted Pella #01754-F) placed on the filter stage of a microorifice uniform deposition impactor (MOUDI) for offline electron microscopy analysis. Computer-controlled scanning electron microscopy (CC-SEM) measurements were performed at the Environmental Molecular Sciences Laboratory (EMSL) at PNNL using a Quanta 3D environmental SEM (FEI) with an Si(Li) detector. Particles were initially imaged in secondary electron and scattered transmitted electron modes, and CC-SEM measurements were acquired at 10,000x magnification in the transmission mode at an accelerating voltage of 20.00 keV. Each spectrum was acquired for 10 seconds. Several steps were taken to filter particles from the raw CCSEM data. First, particles with an average diameter less than 200 nm were removed due to potentially low particle signal at the resolution we used. Second, particles with CPS (counts per second) values <40 were removed due to insufficient signal to adequately determine composition. Third, particles with CPS values >2000 were removed. Fourth, particles with an average diameter <1000 nm and CPS values >1000 were removed. The third and fourth steps are performed to remove particles that are located on or near the copper TEM grid. Copper from the grid can contribute significant signal to particles, resulting in high CPS values while also potentially biasing EDX results. We use two CPS thresholds, for particles >1000 or <1000 nm, when filtering particles to avoid removing larger particles which naturally generate higher CPS values because they contain more material. These data filtering steps were undertaken in consultation with the scientific research staff at EMSL who have extensive expertise in the use of CCSEM and TEM for quantitative aerosol particle analysis. SEM measurements were also performed at CMU using a Quanta 600 SEM equipped with an Everhart-Thornley detector operating in secondary electron mode at an accelerating voltage of 20.00 keV. TEM measurements were acquired at EMSL using a Titan 80-300 scanning/TEM equipped with an Si(Li) detector at an accelerating voltage of 300 keV. Selected area electron diffraction patterns in Fig. 4 had their contrast enhanced within ImageJ software to a normalized saturated pixel ratio of 0.6% to better display the less-intense diffraction spots.

*Data Availability*

The datasets associated with this work will be made available through Carnegie Mellon University's research repository, Kilthub (https://kilthub.cmu.edu), and linked to this publication: doi:10.1184/R1/12693095.

**Acknowledgements.** Libor Kovarik, Swarup China, and the staff at the Environmental and Molecular Sciences Laboratory at Pacific Northwest National Lab assisted with our electron microscopy analysis. Stacy Freitas at the Klamath Basin National Wildlife Refuge Complex in Tulelake, CA and the staff at the University of Florida UF/IFAS Center for Aqueous and Invasive Plants and the Okefenokee and Alligator River National Wildlife Refuges assisted us in acquiring the fuels used. We acknowledge the use of the Materials Characterization Facility at Carnegie Mellon University, supported by the NSF (MCF-677785). This research was supported by the

National Science Foundation (AGS-1552608, CHE-1554941, CBET-1804737). MP was supported by an NSF Graduate Research Fellowship. L. Jahn was partially supported by a Steinbrenner Fellowship from CMU. TB was partially supported by a collaborative student grant from the Department of Mechanical Engineering at CMU. Allen Robinson, Neil Donahue, and Coty Jen provided valuable feedback on an earlier draft of the manuscript.

**Author Contributions.** Conceptualization: RS and MP; Investigation: MP, L. Jahn, L. Jahl, TB, and JS; Formal Analysis: L. Jahn, MP, L. Jahl, TB, RS; Writing – Original Draft: MP, L. Jahn, RS; Writing – Editing: L. Jahn, MP, L. Jahl, TB, RS; Resources: MP, L. Jahl, TB; Supervision: RS.

**Competing interests.** The authors declare no competing interests.

**References**

1. J. Mülmenstädt, O. Sourdeval, J. Delanoë, J. Quaas, Frequency of occurrence of rain from liquid-, mixed-, and ice-phase clouds derived from A-Train satellite retrievals. *Geophys. Res. Lett.* **42**, 6502–6509 (2015).
2. J. Fan, *et al.*, Review of Aerosol–Cloud Interactions: Mechanisms, Significance, and Challenges. *J. Atmos. Sci.* **73**, 4221–4252 (2016).
3. J. H. Seinfeld, *et al.*, Improving our fundamental understanding of the role of aerosol-cloud interactions in the climate system. *Proc. Natl. Acad. Sci. U. S. A.* **113**, 5781–90 (2016).
4. P. J. DeMott, *et al.*, Predicting global atmospheric ice nuclei distributions and their impacts on climate. *Proc. Natl. Acad. Sci. U. S. A.* **107**, 11217–11222 (2010).
5. T. Storelvmo, Aerosol Effects on Climate via Mixed-Phase and Ice Clouds. *Annu. Rev. Earth Planet. Sci.* **45**, 199–222 (2017).
6. M. A. Holden, *et al.*, High-speed imaging of ice nucleation in water proves the existence of active sites. *Sci. Adv.* **5**, eaav4316 (2019).
7. Z. A. Kanji, *et al.*, Overview of Ice Nucleating Particles https:/doi.org/10.1175/AMSMONOGRAPHS-D-16-0006.1.
8. P. J. DeMott, *et al.*, Integrating laboratory and field data to quantify the immersion freezing ice nucleation activity of mineral dust particles. *Atmos. Chem. Phys.* **15**, 393–409 (2015).
9. L. G. Jahn, W. D. Fahy, D. B. Williams, R. C. Sullivan, Role of Feldspar and Pyroxene Minerals in the Ice Nucleating Ability of Three Volcanic Ashes. *ACS Earth Sp. Chem.* **3**, 626–636 (2019).
10. B. J. Murray, D. O'Sullivan, J. D. Atkinson, M. E. Webb, Ice nucleation by particles immersed in supercooled cloud droplets. *Chem. Soc. Rev.* **41**, 6519 (2012).
11. J. Lelieveld, J. S. Evans, M. Fnais, D. Giannadaki, A. Pozzer, The contribution of outdoor air pollution sources to premature mortality on a global scale. *Nature* **525**, 367–371 (2015).
12. G. R. van der Werf, *et al.*, Global fire emissions and the contribution of deforestation, savanna, forest, agricultural, and peat fires (1997–2009). *Atmos. Chem. Phys.* **10**, 11707–11735 (2010).
13. A. L. Hodshire, *et al.*, Aging Effects on Biomass Burning Aerosol Mass and Composition: A Critical Review of Field and Laboratory Studies. *Environ. Sci. Technol.* **53**, 10007–10022 (2019).
14. D. A. Peterson, *et al.*, Wildfire-driven thunderstorms cause a volcano-like stratospheric

injection of smoke. *Clim. Atmos. Sci.* **1**, 30 (2018).
15. G. P. Schill, *et al.*, Widespread biomass burning smoke throughout the remote troposphere. *Nat. Geosci.* **13**, 422–427 (2020).
16. J. Chen, *et al.*, A review of biomass burning: Emissions and impacts on air quality, health and climate in China. *Sci. Total Environ.* **579**, 1000–1034 (2017).
17. R. J. Park, D. J. Jacob, J. A. Logan, Fire and biofuel contributions to annual mean aerosol mass concentrations in the United States. *Atmos. Environ.* **41**, 7389–7400 (2007).
18. I. N. Sokolik, A. J. Soja, P. J. DeMott, D. Winker, Progress and Challenges in Quantifying Wildfire Smoke Emissions, Their Properties, Transport, and Atmospheric Impacts. *J. Geophys. Res. Atmos.* **124**, 13005–13025 (2019).
19. L. M. Zamora, *et al.*, Aircraft-measured indirect cloud effects from biomass burning smoke in the Arctic and subarctic. *Atmos. Chem. Phys.* **16**, 715–738 (2016).
20. Y. Li, Cloud Condensation Nuclei Activity and Hygroscopicity of Fresh and Aged Biomass Burning Particles. *Pure Appl. Geophys.* **176**, 345–356 (2019).
21. M. D. Petters, *et al.*, Ice nuclei emissions from biomass burning. *J. Geophys. Res.* **114**, D07209 (2009).
22. C. S. McCluskey, *et al.*, Characteristics of atmospheric ice nucleating particles associated with biomass burning in the US: Prescribed burns and wildfires. *J. Geophys. Res. Atmos.* **119**, 10458–10470 (2014).
23. B. Ford, *et al.*, Future Fire Impacts on Smoke Concentrations, Visibility, and Health in the Contiguous United States. *GeoHealth* **2**, 229–247 (2018).
24. M. A. Moritz, *et al.*, Climate change and disruptions to global fire activity. *Ecosphere* **3**, art49 (2012).
25. A. G. Hallar, *et al.*, Impacts of increasing aridity and wildfires on aerosol loading in the intermountain Western US. *Environ. Res. Lett.* **12**, 014006 (2017).
26. J. Williams, Exploring the onset of high-impact mega-fires through a forest land management prism. *For. Ecol. Manage.* **294**, 4–10 (2013).
27. V. M. Donovan, C. L. Wonkka, D. Twidwell, Surging wildfire activity in a grassland biome. *Geophys. Res. Lett.* **44**, 5986–5993 (2017).
28. A. Park Williams, *et al.*, The 2016 Southeastern U.S. Drought: An Extreme Departure From Centennial Wetting and Cooling. *J. Geophys. Res. Atmos.* **122**, 10,888-10,905 (2017).
29. A. Woodward, Australia's fires are 46% bigger than last year's Brazilian Amazon blazes. There are at least 2 months of fire season to go. *Insider* (2020).
30. A. J. Prenni, *et al.*, Biomass burning as a potential source for atmospheric ice nuclei: Western wildfires and prescribed burns. *Geophys. Res. Lett.* **39** (2012).
31. E. J. T. Levin, *et al.*, Ice-nucleating particle emissions from biomass combustion and the potential importance of soot aerosol. *J. Geophys. Res. Atmos.* **121**, 5888–5903 (2016).
32. J. Rissler, *et al.*, Hygroscopic Behavior of Aerosol Particles Emitted from Biomass Fired Grate Boilers. *Aerosol Sci. Technol.* **39**, 919–930 (2005).
33. L. S. Johansson, C. Tullin, B. Leckner, P. Sjövall, Particle emissions from biomass combustion in small combustors. *Biomass and Bioenergy* **25**, 435–446 (2003).
34. F. Mahrt, *et al.*, Ice nucleation abilities of soot particles determined with the Horizontal Ice Nucleation Chamber. *Atmos. Chem. Phys.* **18**, 13363–13392 (2018).
35. G. P. Schill, *et al.*, Ice-nucleating particle emissions from photochemically aged diesel and biodiesel exhaust. *Geophys. Res. Lett.* **43**, 5524–5531 (2016).

36. R. Ullrich, *et al.*, A New Ice Nucleation Active Site Parameterization for Desert Dust and Soot. *J. Atmos. Sci.* **74**, 699–717 (2017).
37. R. Wagner, M. Jähn, K. Schepanski, Wildfires as a source of airborne mineral dust - Revisiting a conceptual model using large-eddy simulation (LES). *Atmos. Chem. Phys.* **18**, 11863–11884 (2018).
38. C. B. Clements, S. Zhong, X. Bian, W. E. Heilman, D. W. Byun, First observations of turbulence generated by grass fires. *J. Geophys. Res.* **113**, D22102 (2008).
39. M. B. Bodí, *et al.*, Wildland fire ash: Production, composition and eco-hydro-geomorphic effects. *Earth-Science Rev.* **130**, 103–127 (2014).
40. B. Wang, *et al.*, Airborne soil organic particles generated by precipitation. *Nat. Geosci.* **9**, 433–437 (2016).
41. Y. S. Joung, C. R. Buie, Aerosol generation by raindrop impact on soil. *Nat. Commun.* **6**, 6083 (2015).
42. L. F. Radke, *et al.*, "Particulate and Trace Gas Emissions from Large Biomass Fires in North America" in *Global Biomass Burning: Atmospheric, Climatic, and Biospheric Implications*, (1991), pp. 209–224.
43. M. O. Andreae, *et al.*, Smoking Rain Clouds over the Amazon. *Science (80-. ).* **303**, 1337–1342 (2004).
44. J. S. Schlosser, *et al.*, Analysis of aerosol composition data for western United States wildfires between 2005 and 2015: Dust emissions, chloride depletion, and most enhanced aerosol constituents. *J. Geophys. Res. Atmos.* **122**, 8951–8966 (2017).
45. L. C. Maudlin, Z. Wang, H. H. Jonsson, A. Sorooshian, Impact of wildfires on size-resolved aerosol composition at a coastal California site. *Atmos. Environ.* **119**, 59–68 (2015).
46. S. V. Vassilev, D. Baxter, C. G. Vassileva, An overview of the behaviour of biomass during combustion: Part I. Phase-mineral transformations of organic and inorganic matter. *Fuel* **112**, 391–449 (2013).
47. J. Werkelin, B.-J. Skrifvars, M. Zevenhoven, B. Holmbom, M. Hupa, Chemical forms of ash-forming elements in woody biomass fuels. *Fuel* **89**, 481–493 (2010).
48. H. A. Currie, C. C. Perry, Silica in Plants: Biological, Biochemical and Chemical Studies. *Ann. Bot.* **100**, 1383–1389 (2007).
49. S. V. Vassilev, D. Baxter, L. K. Andersen, C. G. Vassileva, An overview of the chemical composition of biomass. *Fuel* **89**, 913–933 (2010).
50. E. Kirkby, "Introduction, Definition and Classification of Nutrients" in *Marschner's Mineral Nutrition of Higher Plants*, P. B. T.-M. M. N. of H. P. (Third E. Marschner, Ed. (Elsevier, 2012), pp. 3–5.
51. L. L. Baxter, *et al.*, The behavior of inorganic material in biomass-fired power boilers: field and laboratory experiences. *Fuel Process. Technol.* **54**, 47–78 (1998).
52. S. V. Vassilev, D. Baxter, L. K. Andersen, C. G. Vassileva, T. J. Morgan, An overview of the organic and inorganic phase composition of biomass. *Fuel* **94**, 1–33 (2012).
53. V. N. Balfour, S. W. Woods, The hydrological properties and the effects of hydration on vegetative ash from the Northern Rockies, USA. *Catena* (2013) https:/doi.org/10.1016/j.catena.2013.06.014.
54. M. K. Misra, K. W. Ragland, A. J. Baker, Wood ash composition as a function of furnace temperature. *Biomass and Bioenergy* **4**, 103–116 (1993).
55. B. R. Goforth, R. C. Graham, K. R. Hubbert, C. W. Zanner, R. A. Minnich, Spatial

distribution and properties of ash and thermally altered soils after high-severity forest fire, southern California. *Int. J. Wildl. Fire* (2005) https:/doi.org/10.1071/WF05038.
56. R. F. Pueschel, G. Langer, Sugar cane fires as a source of ice nuclei in Hawaii. *J. Appl. Meteorol.* **12**, 549--551 (1973).
57. N. S. Umo, *et al.*, Ice nucleation by combustion ash particles at conditions relevant to mixed-phase clouds. *Atmos. Chem. Phys* **15**, 5195–5210 (2015).
58. S. Grawe, *et al.*, The immersion freezing behavior of ash particles from wood and brown coal burning. *Atmos. Chem. Phys.* **16**, 13911–13928 (2016).
59. C. E. Stockwell, *et al.*, Trace gas emissions from combustion of peat, crop residue, domestic biofuels, grasses, and other fuels: configuration and Fourier transform infrared (FTIR) component of the fourth Fire Lab at Missoula Experiment (FLAME-4). *Atmos. Chem. Phys.* **14**, 9727–9754 (2014).
60. E. E. Knapp, B. L. Estes, C. N. Skinner, Ecological effects of prescribed fire season: a literature review and synthesis for managers. *Gen. Tech. Rep. PSW-GTR-224. Albany, CA U.S. Dep. Agric. For. Serv. Pacific Southwest Res. Stn.*, 1–80 (2009).
61. T. T. van Leeuwen, *et al.*, Biomass burning fuel consumption rates: a field measurement database. *Biogeosciences* **11**, 7305–7329 (2014).
62. H. Beydoun, M. Polen, R. C. Sullivan, Effect of particle surface area on ice active site densities retrieved from droplet freezing spectra. *Atmos. Chem. Phys.* **16**, 13359–13378 (2016).
63. M. Polen, T. Brubaker, J. Somers, R. C. Sullivan, Cleaning up our water: reducing interferences from nonhomogeneous freezing of "pure" water in droplet freezing assays of ice-nucleating particles. *Atmos. Meas. Tech.* **11**, 5315–5334 (2018).
64. S. Grawe, *et al.*, Coal fly ash: linking immersion freezing behavior and physicochemical particle properties. *Atmos. Chem. Phys.* **18**, 13903–13923 (2018).
65. D. J. Losey, S. K. Sihvonen, D. P. Veghte, E. Chong, M. A. Freedman, Acidic processing of fly ash: chemical characterization, morphology, and immersion freezing. *Environ. Sci. Process. Impacts* **20**, 1581–1592 (2018).
66. N. Hiranuma, *et al.*, A comprehensive laboratory study on the immersion freezing behavior of illite NX particles: a comparison of 17 ice nucleation measurement techniques. *Atmos. Chem. Phys.* **15**, 2489–2518 (2015).
67. P. J. DeMott, *et al.*, The Fifth International Workshop on Ice Nucleation phase 2 (FIN-02): laboratory intercomparison of ice nucleation measurements. *Atmos. Meas. Tech.* **11**, 6231–6257 (2018).
68. T. Zolles, *et al.*, Identification of ice nucleation active sites on feldspar dust particles. *J. Phys. Chem. A* **119**, 2692–700 (2015).
69. J. D. Atkinson, *et al.*, The importance of feldspar for ice nucleation by mineral dust in mixed-phase clouds. *Nature* **498**, 355–358 (2013).
70. A. Kumar, C. Marcolli, T. Peter, Ice nucleation activity of silicates and aluminosilicates in pure water and aqueous solutions – Part 2: Quartz and amorphous silica. *Atmos. Chem. Phys.* **19**, 6035–6058 (2019).
71. A. D. Harrison, *et al.*, The ice-nucleating ability of quartz immersed in water and its atmospheric importance compared to K-feldspar. *Atmos. Chem. Phys.* **19**, 11343–11361 (2019).
72. T. F. Whale, M. A. Holden, T. W. Wilson, D. O'Sullivan, B. J. Murray, The enhancement and suppression of immersion mode heterogeneous ice-nucleation by solutes. *Chem. Sci.*

**9**, 4142–4151 (2018).
73. E. Chong, M. King, K. E. Marak, M. A. Freedman, The Effect of Crystallinity and Crystal Structure on the Immersion Freezing of Alumina. *J. Phys. Chem. A* **123**, 2447–2456 (2019).
74. F. Echalar, A. Gaudichet, H. Cachier, P. Artaxo, Aerosol emissions by tropical forest and savanna biomass burning: Characteristic trace elements and fluxes. *Geophys. Res. Lett.* **22**, 3039–3042 (1995).
75. J. Li, M. Pósfai, P. V. Hobbs, P. R. Buseck, Individual aerosol particles from biomass burning in southern Africa: 2, Compositions and aging of inorganic particles. *J. Geophys. Res. Atmos.* **108**, doi: 10.1029/2002JD002310 (2003).
76. A. Gaudichet, *et al.*, Trace elements in tropical African savanna biomass burning aerosols. *J. Atmos. Chem.* **22**, 19–39 (1995).
77. M. Hawkesford, *et al.*, "Functions of Macronutrients" in *Marschner's Mineral Nutrition of Higher Plants*, P. B. T.-M. M. N. of H. P. (Third E. Marschner, Ed. (Elsevier, 2012), pp. 135–189.
78. M. Posfai, R. Simonics, J. Li, P. V Hobbs, P. R. Buseck, Individual aerosol particles from biomass burning in southern Africa: 1. Compositions and size distributions of carbonaceous particles. *J. Geophys. Res.* **108** (2003).
79. L. L. Baxter, Char fragmentation and fly ash formation during pulverized-coal combustion. *Combust. Flame* **90**, 174–184 (1992).
80. L. L. Baxter, Ash deposition during biomass and coal combustion: A mechanistic approach. *Biomass and Bioenergy* **4**, 85–102 (1993).
81. X. Gao, S. Yani, H. Wu, Emission of Inorganic PM 10 during the Combustion of Spent Biomass from Mallee Leaf Steam Distillation. *Energy & Fuels* **29**, 5171–5175 (2015).
82. M. Xu, D. Yu, H. Yao, X. Liu, Y. Qiao, Coal combustion-generated aerosols: Formation and properties. *Proc. Combust. Inst.* **33**, 1681–1697 (2011).
83. Y. Wang, B. Van Devener, X. Li, J. O. L. Wendt, High resolution STEM/EDX spectral imaging to resolve metal distributions within ~100 nm combustion generated ash particles. *Aerosol Sci. Technol.*, 1–12 (2019).
84. W. Yang, *et al.*, Characteristics of Particulate Matter Emitted from Agricultural Biomass Combustion. *Energy & Fuels* **31**, 7493–7501 (2017).
85. R. J. Quann, A. F. Sarofim, A scanning electron microscopy study of the transformations of organically bound metals during lignite combustion. *Fuel* **65**, 40–46 (1986).
86. X. Gao, M. U. Rahim, X. Chen, H. Wu, Significant contribution of organically-bound Mg, Ca, and Fe to inorganic PM10 emission during the combustion of pulverized Victorian brown coal. *Fuel* **117**, 825–832 (2014).
87. R. J. Quann, M. Neville, A. F. Sarofim, A Laboratory Study of the Effect of Coal Selection on the Amount and Composition of Combustion Generated Submicron Particles. *Combust. Sci. Technol.* **74**, 245–265 (1990).
88. S. F. Miller, H. H. Schobert, Effect of the Occurrence and Modes of Incorporation of Alkalis, Alkaline Earth Elements, and Sulfur on Ash Formation in Pilot-Scale Combustion of Beulah Pulverized Coal and Coal-Water Slurry Fuel. *Energy & Fuels* **8**, 1208–1216 (1994).
89. A. Kumar, C. Marcolli, B. Luo, T. Peter, Ice nucleation activity of silicates and aluminosilicates in pure water and aqueous solutions – Part 1: The K-feldspar microcline. *Atmos. Chem. Phys.* **18**, 7057–7079 (2018).

90. D. Huber, V. Römheld, M. Weinmann, “Relationship between Nutrition, Plant Diseases and Pests” in *Marschner’s Mineral Nutrition of Higher Plants*, P. B. T.-M. M. N. of H. P. (Third E. Marschner, Ed. (Elsevier, 2012), pp. 283–298.
91. K. Sekimoto, *et al.*, High-and low-temperature pyrolysis profiles describe volatile organic compound emissions from western US wildfire fuels. *Atmos. Chem. Phys.* (2018) https:/doi.org/10.5194/acp-18-9263-2018.
92. T. C. J. Hill, *et al.*, Sources of organic ice nucleating particles in soils. *Atmos. Chem. Phys.* **16**, 7195–7211 (2016).
93. M. Paramonov, R. O. David, R. Kretzschmar, Z. A. Kanji, A laboratory investigation of the ice nucleation efficiency of three types of mineral and soil dust. *Atmos. Chem. Phys.* **18**, 16515–16536 (2018).
94. Y. Tobo, *et al.*, Organic matter matters for ice nuclei of agricultural soil origin. *Atmos. Chem. Phys.* **14**, 8521–8531 (2014).
95. S. K. Akagi, *et al.*, Emission factors for open and domestic biomass burning for use in atmospheric models. *Atmos. Chem. Phys.* **11**, 4039–4072 (2011).
96. S. L. Gomez, *et al.*, Southwestern U.S. Biomass Burning Smoke Hygroscopicity: The Role of Plant Phenology, Chemical Composition, and Combustion Properties. *J. Geophys. Res. Atmos.* **123**, 5416–5432 (2018).
97. A. E. Barkley, *et al.*, African biomass burning is a substantial source of phosphorus deposition to the Amazon, Tropical Atlantic Ocean, and Southern Ocean. *Proc. Natl. Acad. Sci.*, 201906091 (2019).
98. A. Ito, *et al.*, Pyrogenic iron: The missing link to high iron solubility in aerosols. *Sci. Adv.* **5**, eaau7671 (2019).
99. A. T. Ahern, L. Goldberger, L. Jahl, J. Thornton, R. C. Sullivan, Production of N2O5 and ClNO2 through nocturnal processing of biomass-burning aerosol. *Environ. Sci. Technol.* **52**, 550–559 (2018).
100. M. Polen, E. Lawlis, R. C. Sullivan, The unstable ice nucleation properties of Snomax® bacterial particles. *J. Geophys. Res. Atmos.* **121**, 11,666-11,678 (2016).
101. T. Brubaker, *et al.*, Development and characterization of a “store and create” microfluidic device to determine the heterogeneous freezing properties of ice nucleating particles. *Aerosol Sci. Technol.* **54**, 79–93 (2020).
102. G. Vali, Quantitative Evaluation of Experimental Results on the Heterogeneous Freezing Nucleation of Supercooled Liquids. *J. Atmos. Sci.* **28**, 402–409 (1971).
103. G. Vali, Interpretation of freezing nucleation experiments: singular and stochastic; sites and surfaces. *Atmos. Chem. Phys.* **14**, 5271–5294 (2014).
104. D. O′Sullivan, *et al.*, The relevance of nanoscale biological fragments for ice nucleation in clouds. *Sci. Rep.* **5**, 8082 (2015).

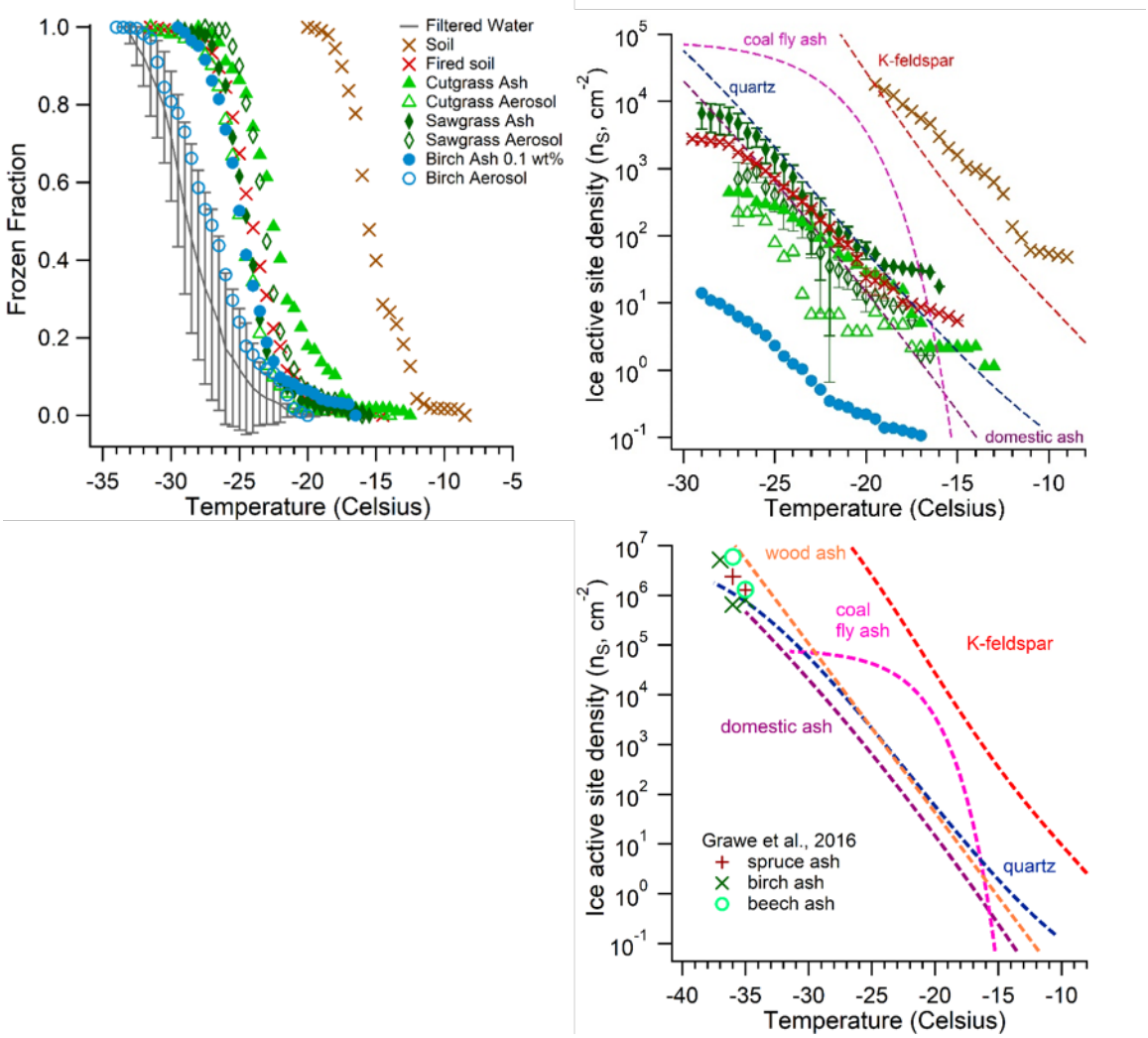


**Figure 1.** Droplet freezing temperature spectra (top left) and ice-active surface site density ($n_s$) spectra (top right) of biomass-burning ash (solid symbols) and aerosol (open symbols) generated from combustion of cutgrass (triangles), sawgrass (diamonds), and birch wood (squares). Also shown are a soil sample from a wetland in North Carolina, the soil exposed to combustion conditions (crosses), and an average filtered water control (grey). Ash and soil suspensions were made at 0.01 weight %, except for birch ash which was analyzed at 0.1 weight %. Aerosol spectra were acquired with 0.5 µL droplets while ash and soil were acquired with 0.1 µL droplets. Each spectrum is the composite of 2-4 separate arrays. Error bars on the pure water background represent a single standard deviation around the average. A representative set of error bars calculated from the variability in the filtered water background freezing spectrum (104) is included for the $n_s$ values of the sawgrass aerosol and ash and fired soil datasets; at many temperatures the error bars are smaller than the symbol size. A complete set of error bars is instead included in SI Appendix Figs. S1, S2, and S5 due to space limitations. Also included here are three $n_s$ (INA) parameterizations for: domestic ash produced from a mixture of hard and soft woods combusted in a domestic heating oven (57), coal fly ash collected from an electrostatic precipitator (57), quartz minerals (71), and highly ice-active potassium feldspar minerals (71). A more complete set of literature $n_s$ parameterizations are shown in the lower panel, incorporating the above-mentioned freezing data and additional data from Umo et al. (57) and Grawe et al. (58). Data from Grawe et al. are from dry-generated size-selected 300 nm bottom ash particles generated in a high-efficiency heating oven. Data from Umo et al. are from the domestic ash and coal fly ash samples. Together with our data this demonstrates that ash particles produced from biomass

combustion are capable of nucleating ice over a wide temperature range similar to other mineral systems such as quartz.

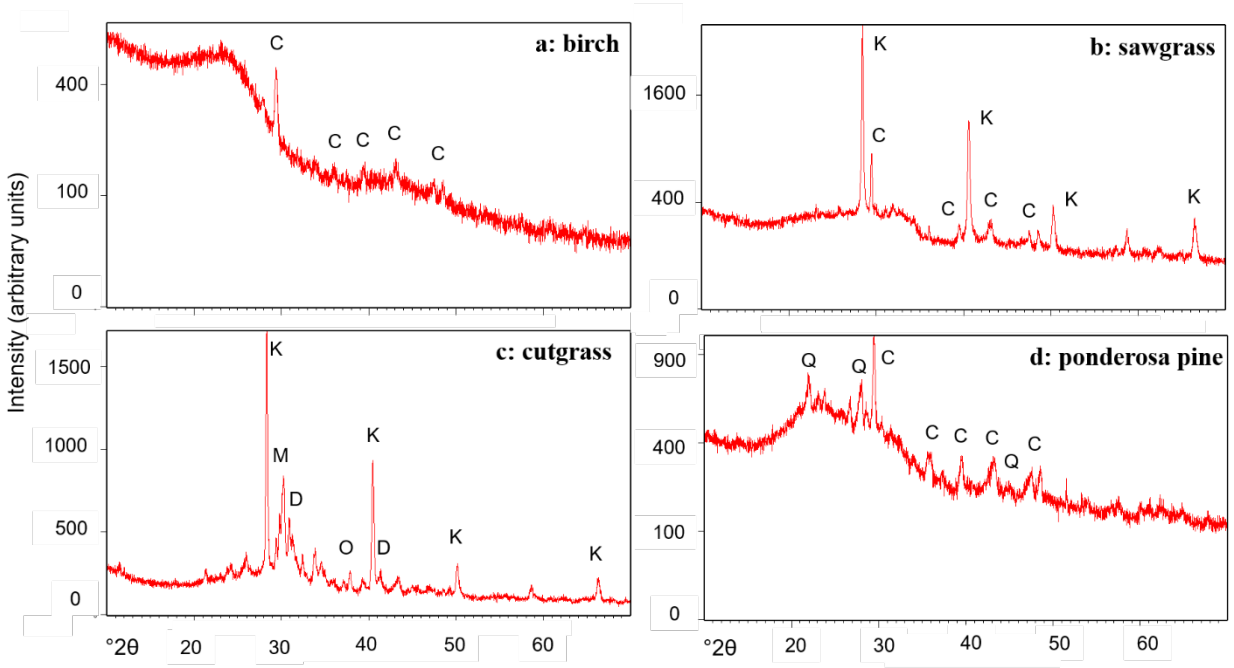


**Figure 2.** X-ray diffraction (XRD) spectra to determine crystalline phase composition acquired from (left-to-right, top-to-bottom) birch, sawgrass, cutgrass, and ponderosa pine bottom ashes. Note the different relative intensity (y-axis) for each spectrum. XRD spectra for switchgrass, wiregrass, and NC grass are shown in the SI Appendix, Fig. S3. Spectra were acquired over the 2θ range of 10-70°. The spectra of the ashes all contain a baseline rise and broad feature at 2θ values less than approximately 40°, indicative of amorphous material. Major spectral features corresponding to crystalline phases are denoted with individual letters as follows: C – calcite, $CaCO_3$; K – sylvite, KCl; M – potassium-sodium sulfate, $(Na,K)SO_4$; D – dolomite, $(Ca,Mg)CO_3$; O – potassium sulfate, $K_2SO_4$; Q – quartz, $SiO_2$; N – halite, NaCl.

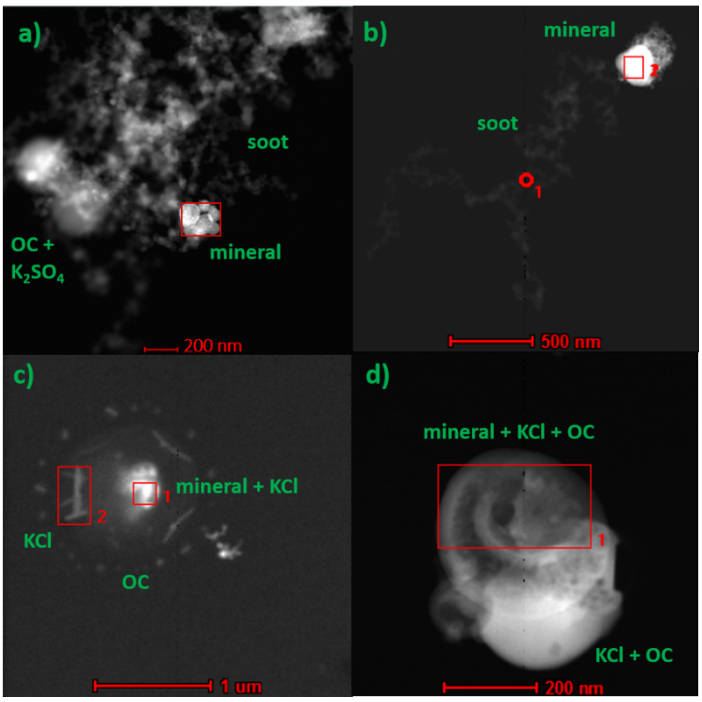


**Figure 3.** TEM images of mineral phases in BBA. Images a) to c) are from ponderosa pine BBA while image d) is from sawgrass BBA. The mineral and other particle regions were categorized by chemical composition based on energy dispersive X-ray (EDX) spectroscopy and morphology; these are labelled in the TEM images. The magnification and scale bars are variable as indicated. EDX spectra for the areas outlined in red are shown in the SI Appendix, Fig. S4 and show that the mineral region in a) is composed mostly of iron, silicon, and oxygen with smaller contributions from sulfur, sodium, potassium, magnesium, zinc, and manganese; the region in b) is composed of iron and oxygen; the region in c) is composed of magnesium, aluminum, silicon, and oxygen; and the region in d) is composed of silicon, sodium, and oxygen.

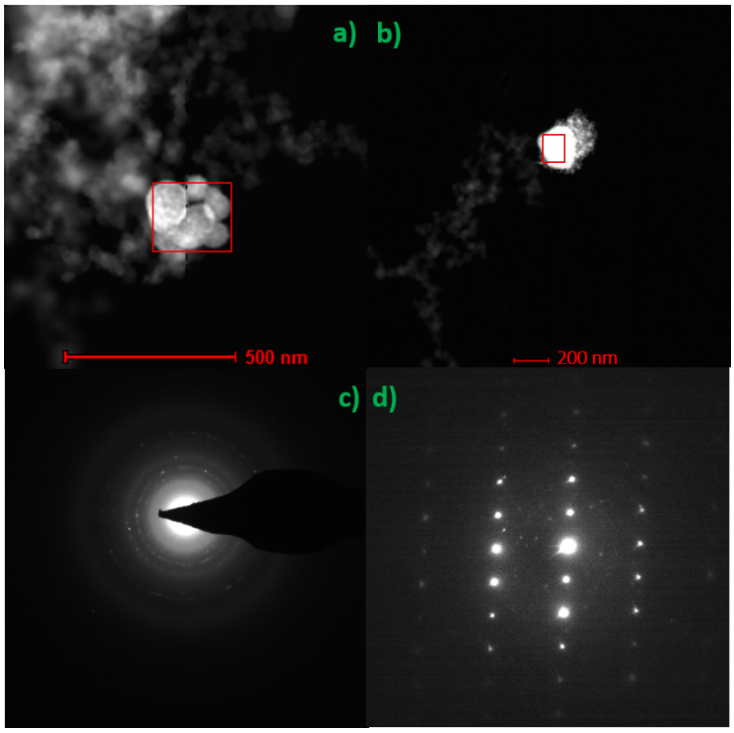


**Figure 4.** Transmission electron microscopy (TEM) images (top, a & b) and corresponding selected area electron diffraction (SAED) patterns (bottom, c & d) for two aerosols samples generated from the combustion of ponderosa pine needles. The SAED patterns correspond to the areas in the upper images indicated by a red box. The regular and intense bright spots in the SAED pattern in d) indicates the main particle is a single well-formed crystal, and the less intense spots originate from a large agglomeration of small iron oxide particles around the upper right edge of the main particle in b). The many rings and spots in the SAED pattern in c) indicate that this region is composed of disordered crystalline, polycrystalline, and/or amorphous phases. Scale bars are 500 nm (left) or 200 nm (right) long.

**Table 1.** Biomass fuel and ash properties.[1]

| Sample: Ash (Fuel) | Birch Wood | Cutgrass | NC grass | Switchgrass | Wiregrass |
|---|---|---|---|---|---|
| $n_s$(–17 °C) | 0.11(0) | 5.07(2.16) | 2.74(n/a) | 1.65(38.03) | 1.31(4.90) |
| $n_s$(–24 °C) | 1.24(0) | 184.2(57.98) | 103.3(n/a) | 37.75(0) | 6.25(1062) |
| BET SSA ($m^2$ $g^{-1}$) | 275.58 | 16.83 | 20.76 | 37.84 | 102.35 |
| Ash % w/w[2] | 0.26 | 6.27 | 5.34 | 4.87 | 1.74 |
| Total Carbon % | 80.01 | 5.87 | 22.95 | 30.78 | n/a |
| Tot $CO_2$ as C% | 0.15 | 1.49 | 0.58 | 0.44 | n/a |
| Organic C%[3] | 79.86 | 4.38 | 22.37 | 30.34 | n/a |
| Sodium (µg/g ash) | 211 (<10) | 6990 (1050) | 78600 (9580) | 867 (82) | n/a (149) |
| Magnesium | 1420 (145) | 14400 (866) | 17900 (1950) | 4660 (573) | n/a (438) |
| Potassium | 3690 (470) | 275000 (19700) | 56600 (6180) | 35200 (1750) | n/a (606) |
| Calcium | 7550 (745) | 49000 (2350) | 11900 (1070) | 21900 (2120) | n/a (1410) |
| Aluminum | < 10 (<10) | 347 (28) | 8270 (114) | 462 (47) | n/a (36) |
| Silicon | 105 (226) | 117000 (10100) | 127000(6560) | 198000 (16700) | n/a (6120) |
| Phosphorus | 501 (61) | 24400 (1560) | 9040 (1300) | 9040 (420) | n/a (229) |
| Sulfur | 215 (50) | 12600 (1090) | 14000 (2830) | 1110 (337) | n/a (304) |
| Iron | 39 (5) | 895 (46) | 3400 (89) | 561 (62) | n/a (18) |

[1] $n_s$ values for each fuel are shown in the format ash(aerosol) at –17 °C and –24 °C. Ash composition is shown on the left of each column and the base fuel composition is shown in parentheses on the right. Elements are reported as µg per gram of ash. Brunauer-Emmett-Teller SSA was measured through nitrogen gas adsorption (see Methods).

[2] The quantity "ash" is a percentage that is calculated by weighing the material remaining following combustion and dividing this quantity by the initial weight of the material. This shows the relative amount of refractory material that remains following combustion, on a per mass basis. This quantity will likely vary with fuel composition, temperature and combustion conditions.

[3] Organic carbon was determined by difference between total carbon and inorganic carbonate carbon (tot $CO_2$ as C%).